




Hybrid nanomaterial from pyrolyzed biomass and Fe₃O₄ magnetic nanoparticles for the adsorption of textile dyes

Rízia Keila do Nascimento · Barbara Souza Damasceno · Arthur Nascimento de Melo · Paulo Henrique Miranda de Farias · Jorge Vinícius Fernandes Lima Cavalcanti · Deivson Cesar Silva Sales · Eduardo Henrique Lago Falcão · Ana Cláudia Vaz de Araújo 

Received: 12 April 2022 / Accepted: 24 November 2022 / Published online: 7 December 2022
© The Author(s), under exclusive licence to Springer Nature B.V. 2022

Abstract Industrial dyes are harmful compounds often present in wastewater. In this work, a magnetic nanohybrid material (HB) was hydrothermally synthesized from pyrolyzed sugarcane straw (CN) and magnetic iron oxide nanoparticles. The material was characterized by XRD, FTIR, SEM, TGA, and PZC, and tested for the adsorptive removal of congo red (CR) and indigo carmine (IC) dyes from aqueous solutions at pH 7.0 and 10.0, respectively. The kinetics of adsorption was well explained by both the pseudo-second order (PSO) model ($R_{adj}^2 \sim 0.99$ for CR, 0.96 for IC) and the Elovich model ($R_{adj}^2 \sim 0.98$ for CR, 0.98 for IC). After 24 h, the maximum adsorption capacities of the material were ~ 18.39 mg g⁻¹ for CR and ~ 1.46 mg g⁻¹ for IC.

Adsorption isotherms were obtained at 25, 35, and 45 °C, and four different models were tested. The Sips model, which combines Langmuir and Freundlich, was used to fit the data. HB exhibited greater performance removing CR dye (%R $\sim 72\%$) than IC (%R $\sim 27\%$), therefore suggesting great potential as an adsorbent for CR from wastewater.

Keywords Adsorption · Biomass · Sugarcane · Magnetic nanoparticles · Nanohybrid · Dyes

Introduction

Industrial wastewaters often include hazardous residues, which can reach the environment due to

Rízia Keila do Nascimento and Barbara Souza Damasceno have contributed equally to this work.

Supplementary Information The online version contains supplementary material available at <https://doi.org/10.1007/s10570-022-04978-9>.

R. K. do Nascimento · A. N. de Melo · A. C. V. de Araújo (✉)
Unidade Acadêmica do Cabo de Santo Agostinho,
Universidade Federal Rural de Pernambuco, Pernambuco,
Brazil
e-mail: claudia.vaz@ufrpe.br

B. S. Damasceno
Laboratório de Plasmas e Processos, Instituto Tecnológico
da Aeronáutica, São Paulo, Brazil

P. H. M. de Farias · J. V. F. L. Cavalcanti
Departamento de Engenharia Química, Universidade
Federal de Pernambuco, Pernambuco, Brazil

D. C. S. Sales
Escola Politécnica, Universidade de Pernambuco,
Pernambuco, Brazil

E. H. L. Falcão
Departamento de Química Fundamental, Universidade
Federal de Pernambuco, Pernambuco, Brazil

improper disposal (Damasceno et al. 2020; Shrestha 2021). These pollutants may contain organic dyes, alkaline reagents, soaps, detergents, oils, suspended solids, and others, which create a damaging effect on the aquatic plants' photosynthesis even at low concentrations (Poolwong et al. 2021; Yağmur and Kaya 2021).

Textile wastewaters are usually treated before being discharged (Srinivasan and Viraraghavan 2010). However, these wastewaters may still contain dyes in various concentrations because of their stability (Godoy-Jr et al. 2020; Poolwong et al. 2021; Shrestha 2021). These dyes can be toxic and carcinogenic, causing problems for the environment and the surrounding community (Damasceno et al. 2020; Yağmur and Kaya 2021).

Various physical, chemical, and biological procedures have been proposed and addressed for wastewater treatment (Srinivasan and Viraraghavan 2010; Poolwong et al. 2021; Shrestha 2021). Among them, the adsorption method is highly considered as a viable process because it is facile, cheap, and efficient, and generates relatively small amounts of by-products (Srinivasan and Viraraghavan 2010; De Gisi et al. 2016; Hasanpour and Hatami 2020; Damasceno et al. 2020; Hasanpour et al. 2021b, a).

Dye adsorption is well-established in many adsorbents like graphene, activated carbon, and iron oxide nanoparticles (Srinivasan and Viraraghavan 2010; De Gisi et al. 2016; Damasceno et al. 2020). Concerning the development of new adsorbents, some materials from biomass residues such as sugarcane straw or

bagasse, rice straw, egg and coconut shells, and cattle manure have been widely studied (De Gisi et al. 2016; Bedia et al. 2018). These materials, after proper treatment, present active areas and surface charges compatible with the adsorbates, favoring their removal (Libra et al. 2011). However, the recovery of these adsorbents is necessary to avoid secondary contamination. Magnetic iron oxide nanoparticles (NPs) are a useful class of material to incorporate this functionality into organic adsorbents (Damasceno et al. 2020; Nordin et al. 2021).

Herein, we report the feasibility of using a nanohybrid material (HB) synthesized from sugarcane straw (CN) and iron oxide NPs for removing contaminants from water. We carried out kinetic and thermodynamic studies on the adsorption of two commonly used dyes (congo red, CR, and indigo carmine, IC) to evaluate the behavior of HB and to demonstrate its potential in such applications.

Experimental

Chemicals

The chemicals used in this work are listed in Table 1. They were reagent-grade, commercially available, and were used as received. Distilled water or buffer solution were used in preparing all solutions.

Table 1 Information on reagents used in this work

Reagent name	Molecular formula	Provider	CAS number
Iron(II) sulfate heptahydrate (99%)	FeSO ₄ ·7H ₂ O	Vetec	7782-63-0
Sulfuric acid (95–98%)	H ₂ SO ₄	Vetec	7664-93-9
Sodium hydroxide (98%)	NaOH	Riedel-de Haën	1310-73-2
Hydrochloric acid (34–37%)	HCl	Cinética Química	7647-01-0
Congo red dye (35%)	C ₃₂ H ₂₂ N ₆ Na ₂ O ₆ S ₂	Sigma-Aldrich	573-58-0
Indigo carmine dye (85%)	C ₁₆ H ₈ N ₂ Na ₂ O ₈ S ₂	Sigma-Aldrich	860-22-0
D-(+)-Glucose (≥99.5% (GC))	C ₆ H ₁₂ O ₆	Sigma-Aldrich	492-62-6
D-(+)-Xylose (≥99%)	C ₅ H ₁₀ O ₅	Sigma-Aldrich	58-86-6
5-(Hydroxymethyl)furfural (analytical standard)	C ₆ H ₆ O ₃	Sigma-Aldrich	67-47-0
Buffer sol. of disodium phosphate/potassium phosphate monobasic (pH 7.0)	–	Neon	–
Buffer sol. of boric acid/potassium chloride (pH 10.0)	–	Neon	–

Synthesis of magnetic iron oxide nanoparticles

Magnetic iron oxide nanoparticles were prepared by the coprecipitation method. First, 90 mL of 0.01 mol L⁻¹ aqueous solution of ferrous sulfate and 5 drops of 0.1 mol L⁻¹ aqueous sulfuric acid were mixed in a beaker. The mixture was sonicated at 60 °C, with slow, continuous dripping of 60 mL of 1.0 mol L⁻¹ aqueous NaOH for 1 h. The solution was heated in a water bath at 100 °C for 20 min. The precipitated NPs were washed three times with 0.01 mol L⁻¹ aqueous HCl, centrifuged at 2500 rpm for 10 min, and dried in an oven at 80 °C for 24 h. The synthesis was performed in triplicate.

Treatment of sugarcane straw

Sugarcane straw was collected in Cabo de Santo Agostinho-PE, washed with 500 mL of distilled water, dried at room temperature (RT), and cut into small pieces. Then, 0.5 g of CN was mixed with 300 mL of distilled water and heated at 80 °C for 20 min. After treatment, the mixture was transferred to a blender and crushed for 10 s. The straw was filtered, dried in an oven at 80 °C for 5 h, and stored in falcon tubes. These experiments were done in duplicate.

Synthesis of magnetic nanohybrid material

The magnetic nanohybrid material was obtained by the hydrothermal method. A mixture of 0.04 g of CN and 0.01 g of NPs was placed in a 22 mL hydrothermal reactor with 10 mL of distilled water, sealed and kept at 150 °C for 48 h. The resulting material was filtered, dried, and packaged in Eppendorf tubes. These experiments were done in duplicate.

Congo red and indigo carmine dyes

The congo red and indigo carmine dyes were used as model contaminants to assess the HB adsorption activity. The CR and IC molar masses are 696.67 g mol⁻¹ and 466.36 g mol⁻¹, respectively. Their chemical structures are shown in Fig. 1.

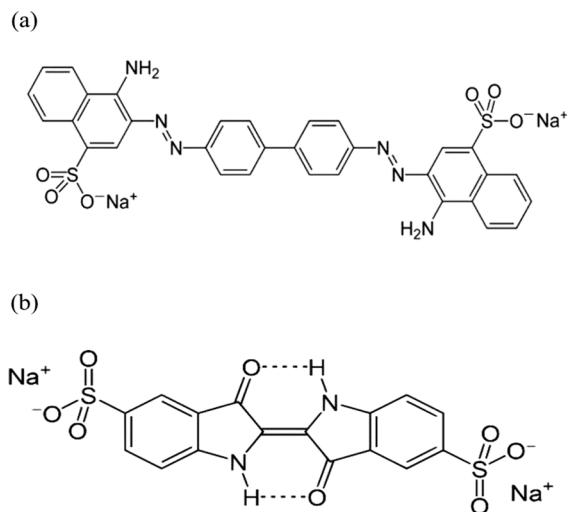


Fig. 1 Chemical structure of **a** congo red dye (CR) and **b** indigo carmine dye (IC)

Characterization

A Panalytical Empyrean X-ray diffractometer (Cu K α line, 0.1542 nm, Bragg–Brentano configuration, 2 θ from 10 to 80°, step size 0.02°, scanning speed 2° min⁻¹) was used for the diffraction experiments at RT. The crystalline phases were indexed using the crystallographic files from the ICSD database. The average crystallite size (D_c) of the NPs was calculated using the Scherrer formula (Cullity and Stock 2014). All samples were thoroughly ground prior to the measurements.

The FTIR spectra were obtained with a Bruker IFS-66 spectrometer. The results were analyzed via Bruker's Spectroscopic Software OPUS. Samples were prepared using KBr pellet.

Sample morphology and approximate elemental composition were evaluated with a Tescan Vega3 scanning electron microscope (SEM) equipped with an energy dispersive spectrometer (EDS).

Thermogravimetric analyses were carried out with a Netzsch STA 449 F3 Jupiter equipment, under nitrogen atmosphere, from 25 °C up to 900 °C, with a heating rate of 5 °C min⁻¹.

The point of zero charge of HB was determined by placing 10 mg of HB in 10 mL of 0.1 mol L⁻¹ NaCl aqueous solutions and stirring for 60 min at 700 rpm. The pH was ranged from 2.0 to 11.0

($\Delta\text{pH} \sim 1.0$). These solutions were adjusted with HCl or NaOH (0.1 mol L^{-1}) (Damasceno et al. 2020). Then, the solutions were separated from the HB material, via an external magnetic field, and the final pH of the supernatant liquid was measured using a pHmeter (MedBio model PHS-3C). The PZC was determined from a plot of final pH versus initial pH. These experiments were done in duplicate.

Nanohybrid material (HB) characterization

For pretreatment, the material was stirred in distilled water for 30 min at $50 \text{ }^\circ\text{C}$, vacuum filtered and dried in an oven at $50 \text{ }^\circ\text{C}$. For the hydrolysis step, 0.4 g of the sample to be analyzed was mixed with 10 mL of 72% sulfuric acid and stirred vigorously for 7 min at $45 \text{ }^\circ\text{C}$. Then, 275 mL of distilled water was added, the solution was transferred to an Erlenmeyer flask, and heated for 30 min in an autoclave at $121 \text{ }^\circ\text{C}$. After cooling, the system was filtered, and the two phases (filtrate and precipitate) were stored separately.

The precipitate was washed with 1.5 L of distilled water, dried in an oven at $60 \text{ }^\circ\text{C}$, and weighed. This dry precipitate is the insoluble lignin fraction. The solid is then transferred to a crucible and heated to $600 \text{ }^\circ\text{C}$ for two hours in a furnace. The ash residue was weighed and its percentage in relation to the initial mass was calculated.

The filtrate was analyzed (high performance liquid chromatography, HPLC) to obtain the amounts of glucose and xylose. A Varian HPLC equipment with a refractive index detector was used. The mobile phase was ultrapure water, acidified in 4 mM of sulfuric acid, with a flow rate of 0.8 mL min^{-1} . The column used was an AMINEX-HPX87-H, heated to $50 \text{ }^\circ\text{C}$. Calibration curves were obtained for glucose and xylose, and their concentrations were determined, calculating the percentage of cellulose and hemicellulose using Eqs. (1) and (2) below:

$$\text{Mass of cellulose} = 0.9 \times \text{mass of glucose} \quad (1)$$

$$\text{Mass of hemicellulose} = 0.88 \times \text{mass of xylose} \quad (2)$$

The filtrate was also analyzed by UV–Vis spectroscopy to check for soluble lignins. These experiments were done in duplicate.

Adsorption experiments of CR and IC dyes onto HB

Dye stability as a function of varying pH was studied by dissolving the dye in aqueous solutions and adjusting the pH with NaOH or HCl solutions. After determining the working pH, the adsorption experiments were performed. From this point on, the CR and IC solutions were prepared with pH 7.0 and pH 10.0 buffer solutions, respectively (see Table 1). Both series of experiments were evaluated by spectrophotometry in the UV–Vis region with a double-beam N6000/N6000PLUS YK Scientific Instrument spectrophotometer, equipped with a tungsten lamp.

For the adsorption kinetic studies, $\sim 10 \text{ mg}$ of the HB material was weighed into different erlenmeyer flasks, and 50 mL of CR (50 mg L^{-1}) or IC (10 mg L^{-1}) dye solutions were added. The flasks were placed in a MARCONI MA 420 incubator with orbital shaker, set to 700 rpm and $24 \text{ }^\circ\text{C}$ for up to 168 h. These experiments were done in duplicate.

For the adsorption equilibrium studies, a series of erlenmeyer flasks with 50 mL of adsorbate solutions with initial concentrations ranging from 5 to 70 mg L^{-1} for CR and from 5 to 50 mg L^{-1} for IC were prepared. Then, the required amount of HB was added, and the flask was shaken at 700 rpm during the optimized equilibrium time. This experiment was carried out at three different temperatures ($25 \text{ }^\circ\text{C}$, $35 \text{ }^\circ\text{C}$, and $45 \text{ }^\circ\text{C}$) for determining the thermodynamic parameters. Two isotherms were obtained in each temperature.

At the end of each adsorption experiment, the adsorbent was removed with an external magnet field and the solutions were analyzed by UV–Vis spectroscopy. The adsorption capacity (Q_m) and the adsorption efficiency (%R) for the HB/CR and HB/IC systems were calculated according to Eqs. (3) and (4).

$$Q_m = q_t = \frac{(C_0 - C_t)V}{m} \quad (3)$$

$$\%R (\%) = \frac{(C_0 - C_t)}{C_0} \times 100 \quad (4)$$

In these equations, Q_m (mg g^{-1}) is the maximum adsorption capacity, q_t (mg g^{-1}) is the adsorption capacity at time t (h). C_0 and C_t (mg L^{-1}) are the initial concentration and the remaining concentration at a specific time, respectively. V (L) is the volume of

the working dye solution, and m (g) is the amount of adsorbent used for the adsorption tests. These experiments were done in duplicate.

Data analysis

The following models were employed to fit the kinetic data: pseudo-first-order (PFO), pseudo-second-order (PSO), Elovich, and the phenomenological internal mass transfer (IMT) and external mass transfer (EMT) models (Wang and Guo 2020).

From these models, it is possible to establish the adsorption rate and to gain insight into the adsorption mechanism. Equations (5) to (9) represent the non-linear PFO, non-linear PSO, Elovich, IMT, and EMT models, respectively:

$$q_t = q_1 (1 - e^{-k_1 t}) \quad (5)$$

$$q_t = \frac{k_2 q_2^2 t}{(1 + k_2 q_2 t)} \quad (6)$$

$$q_t = \frac{1}{b} \ln(1 + abt) \quad (7)$$

$$\frac{dq_t}{dt} = k_{int} \left[\frac{q_3 K_L}{1 + K_L(C_0 - m_{q_t}/V)} - q_t \right] \quad (8)$$

$$\frac{dq_t}{dt} = k_{ext} \left[C_0 - \frac{m_{q_t}}{V} - \frac{q_t}{K_L(q_4 - q_t)} \right] \quad (9)$$

In these equations, q_t (mg g^{-1}) is the adsorption capacity at time t (min), q_1 , q_2 , q_3 , and q_4 (mg g^{-1}) are the maximum amount of adsorbed dye. The terms k_1 (min^{-1}) and k_2 ($\text{g mg}^{-1} \text{s}^{-1}$) are adsorption rates for the PFO and PSO models, respectively. a and b are parameters of Elovich model; K_L (L mg^{-1}) is the equilibrium constant (related to adsorption Langmuir model); k_{int} (min^{-1}) is the internal mass transfer rate constant; and k_{ext} ($\text{L g}^{-1} \text{min}^{-1}$) is the universal external mass transfer coefficient. The unknown parameters were determined by nonlinear regression or minimization of the objective function (ode models): $f_{obj} = \sum (q_{t,exp} - q_{t,calc})^2$, where $q_{t,exp}$ (mg g^{-1}) and $q_{t,calc}$ (mg g^{-1}) are the experimental and determined by models adsorbed amounts at t , respectively.

Adsorption isotherms were used to assess the relationship between solute concentration and the quantity of adsorbate molecules on the solid phase when the equilibrium is reached. The following models were adjusted to the experimental isotherm data: Langmuir, Freundlich, Temkin, and Sips. These models are described by Eqs. (10) to (13), respectively:

$$q_e = \frac{q_{mL} K_L C_e}{1 + K_L C_e} \quad (10)$$

$$q_e = K_F C_e^{1/n_F} \quad (11)$$

$$q_e = B \ln(K_T C_e) \quad (12)$$

$$q_e = \frac{q_{mS} (K_S C_e)^{1/n_S}}{1 + (K_S C_e)^{1/n_S}} \quad (13)$$

In these equations, q_e is the amount of dye adsorbed per gram of adsorbent at equilibrium (mg g^{-1}), q_{mL} and q_{mS} are the maximum coverage capacity of the monolayer for Langmuir and Sips models (mg g^{-1}), respectively, and C_e is the equilibrium concentration of the adsorbate (mg L^{-1}). K_L , K_F , K_T and K_S are the Langmuir (L mg^{-1}), Freundlich ($(\text{mg g}^{-1})(\text{L mg}^{-1})^{1/n}$), Temkin (L g^{-1}) and Sips (L mg^{-1}) isotherm constants. The empirical parameter n_F is related to the adsorption intensity, while n_S is related to heterogeneity of surface of adsorbent. B is a constant related to sorption heat (J mol^{-1}), calculated from RT/b , in which R is the universal gas constant ($8.314 \text{ J mol}^{-1} \text{ K}^{-1}$), T (K) is the temperature, and the magnitude of b is obtained from the plotted curves.

The Langmuir isotherm (Eq. (10)) assumes a monolayer adsorption mechanism. The separation factor (R_L), obtained from the Langmuir isotherm, is used to assess the favorability of the adsorption activity. It designates the shape of the isotherm and can be obtained from Eq. (14).

$$R_L = \frac{1}{1 + K_L C_0} \quad (14)$$

If R_L equals zero, the process is considered irreversible; if it equals one, the process is linear. An R_L between zero and one indicates a favorable process, and if it is greater than one that means that it

is unfavorable (Hall et al. 1966; McKay et al. 1982; Ajenifuja et al. 2017; Hu et al. 2018).

The Freundlich isotherm (Eq. (11)) assumes multilayer adsorption on a heterogeneous surface. The n_F value in this isotherm aids in understanding the favorability of the adsorption mechanism. For $n_F > 1$, adsorption is favorable.

The Temkin model (Eq. (12)) considers the adsorbent-adsorbate interactions and assumes that the adsorption heat drops linearly as adsorption increases. It calculates a uniform binding energy distribution over the quantity of surface binding sites.

The Sips model is a combination between the Langmuir and Freundlich models. For $n_S = 1$, the isotherm shows a Langmuir behavior. If $n_S < 1$ the isotherm presents a rectangular shape (fast equilibrium), and if $n_S \gg 1$ the isotherm reaches the equilibrium at low adsorbate concentration, behaving like a Freundlich isotherm.

To assess the reliability of the models fitted to the adsorption data by nonlinear regression, the adjusted determination coefficient values (R_{adj}^2) and root mean squared error (RMSE) were evaluated and compared. The closer R_{adj}^2 to 1 and lower RMSE values, the greater the agreement of experimental and theoretical data.

The thermodynamic parameters—Gibbs free energy (ΔG^0), adsorption enthalpy (ΔH^0), and entropy (ΔS^0)—were determined by Eq. (15), considering the adsorption isotherms at 25, 35, and 45 °C.

$$\Delta G_i^0 = -RT \ln K_i, \quad \Delta G_i^0 = \Delta H_i^0 - T\Delta S_i^0 \quad (15)$$

In this equation, K_i is the isotherm constant (as in Eqs. (10)–(13)), and R, T are the gas constant and the temperature (in K), as defined previously.

Results and discussion

The synthesized samples were obtained in the form of dark powders, which responded to the application of an external magnetic field. The characterization and adsorption data of each material will be discussed below.

Characterization

Analysis of cellulose

Table 2 shows the fractions of cellulose, hemicellulose, and lignin for CN and HB. For comparison, the table also shows data from hydrothermally treated sugarcane straw samples.

For the monosaccharide analysis, we found that CN contains about 41% of glucose, 24.6% of xylose, and 3.2% of arabinose. Other monosaccharides were detected either in trace amounts (ramnose and fucose) or not detected at all. All these percent values decrease for HB: 26.0 and 12.5% for glucose and xylose, respectively, and only traces of arabinose and others. This decrease is expected because of the hydrothermal treatment (which decomposes some organic fraction) and the addition of the inorganic component when synthesizing the nanohybrid. It

Table 2 Chemical composition (weight %) results for CN and HB

Component	CN	HB	Hydrothermally treated sugarcane straw*
Glucose	41.0	26.0	
Cellobiose	Not detected	Not detected	
Xylose	24.6	12.5	
Arabinose	3.2	Traces	
Fucose, ramnose	Traces	Traces	
Others	Not detected	Not detected	
Total Cellulose	37	23	34–43
Total hemicellulose	24	11	23–38
Total lignin	12	22	11–25
Ashes	5	8	–

* dos Santos Rocha et al. (2017a)

is worth mentioning that glucose and xylose are the major components of cellulose and hemicellulose, respectively, and that the values found are within the expected ranges. From these values, the amount of cellulose and hemicellulose in CN and HB were calculated, according to Eqs. (1) and (2).

The decrease in the fraction of cellulose and hemicellulose in HB in relation to CN must be due to the hydrolysis of these components during the hydrothermal process. It is also clear that the fact that HB is a composite, with a fraction of iron oxide NPs, should contribute to an overall decrease of the organic fraction in general. In any case, it is worth noting that the cellulose:hemicellulose ratio in HB is different from the ratio in CN. This result suggests that, under the conditions used in this work, the decomposition of hemicellulose in CN is more pronounced than the decomposition of cellulose.

On the other hand, the fraction of lignin seems to increase in HB. We believe that this is because the analysis used measures the insoluble fraction of the sample, and in the case of HB the NPs will contribute to this fraction. This is also the likely reason for the increase in the ash content of HB in comparison to CN. We point out that the results for CN agree with values reported by Dos Santos Rocha et al. (2017a) for sugarcane straw treated hydrothermally.

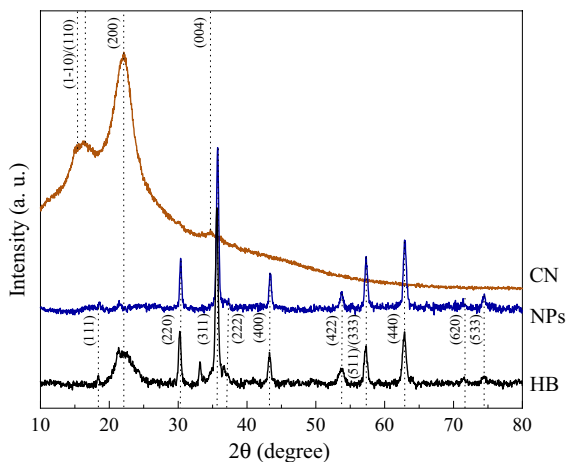


Fig. 2 XRD pattern for pure NPs, CN, and HB material

Table 3 Comparison of calculated and experimental XRD results for the iron oxide NPs

Miller INDICES ^a	2θ (°)		Relative intensity ^b
	Calculated ^a	Found ^b	
(111)	18.45	18.49	3.20
(220)	30.36	30.36	30.82
(311)	35.76	35.73	100.0
(222)	37.41	37.45	3.51
(400)	43.47	43.38	23.02
(422)	53.94	53.75	10.04
(333), (511)	57.51	57.32	30.56
(440)	63.16	62.93	41.63
(620)	71.69	71.56	3.93
(533)	74.76	74.47	7.85

^aFrom CIF for magnetite, ICSD 77591

^bExperimental results from this work

XRD analysis

Figure 2 shows the X-ray diffractograms for pure nanoparticles, treated sugarcane and the nanohybrid material. For the pure NPs, a series of signals matching the pattern of magnetite Fe_3O_4 (ICSD_Coll-Code77591, space group Fd-3 m, $a=8.32 \text{ \AA}$) can be clearly seen. The Miller indices for the signals are also shown in Fig. 2. Table 3 lists the Miller indices, experimental positions, and relative intensities of the magnetite XRD peaks. For comparison, the positions derived from the crystallographic file are also listed. A few reflections were not observed in the experimental pattern, but inspection of the intensities from the crystallographic file confirms that their expected intensities are less than 1% of the most intense peak (311). The average crystallite size (D_c) was estimated from the Scherrer formula (Cullity and Stock 2014) to be $26.2 \pm 2.5 \text{ nm}$. The pattern also showed a weak signal around 34° , which could not be fitted to the magnetite phase. It is likely due to a small fraction of iron oxide changing to hematite during the NPs synthesis.

For the CN materials it is possible to see the weak broad peaks at 15° and 22° , characteristic of cellulose (Marković et al. 2015). The XRD pattern of CN shows the characteristic peaks of type I cellulose, with 2θ values of 16.34° , 22.11° , and 34.58° . These values are very close to the ones reported previously (Li et al. 2008; Phat et al. 2022), at 16.45° , 22.38° , and 34.39° , respectively. The 16.34° signal might

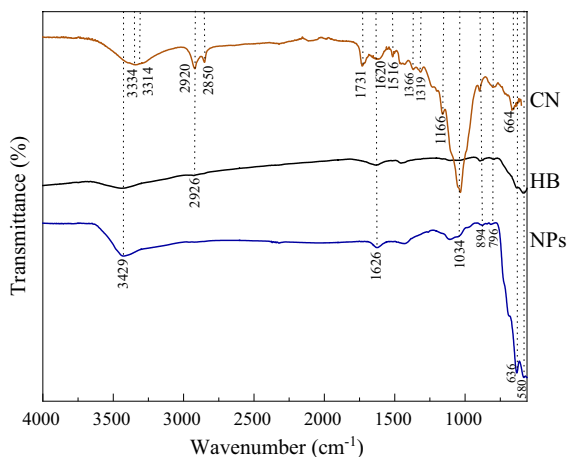


Fig. 3 FTIR spectra for NPs, CN, and HB material

result from an overlap between the (1–10) and (110) planes (French 2014; Shao et al. 2021). The peak at 34.58° is assigned to the (004) plane, while the strongest peak, at 22.11° , corresponds to the (200) plane. These peaks point to the ordered crystal structure in cellulose (French 2014; Phat et al. 2022).

The pattern from the HB material shows the relatively well-defined (albeit weak) peaks from magnetite and the broad, low angle signals from CN. Therefore, the XRD patterns showed that a hybrid material, composed of the NPs and CN, was obtained.

FTIR spectroscopy

Figure 3 shows the infrared spectra for NPs, CN and HB. The characteristic band of the O–H vibration stretching, between 3400 and 3300 cm^{-1} , appears in the spectra for all materials. This indicates the presence of adsorbed water. For the pure nanoparticles, peaks around 580 and 636 cm^{-1} are observed, which are assigned to iron oxide (Fe–O) vibrational stretching modes (Cornell and Schwertmann 2003).

For CN, the spectrum shows the O–H band at 3334 cm^{-1} and the C–H bands at 2920 and 2850 cm^{-1} , as expected for cellulose (Liao et al. 2011; Marković et al. 2015; Lopičić et al. 2019). The band at 1731 cm^{-1} is due to the carbonyl group (C=O) stretching vibration related to hemicellulose (Ahmad et al. 2018), while the bands in the 1160 – 1030 cm^{-1} region are typically attributed to C–O–C groups of the lignocellulosic complex (Siddiqui et al. 2018) and

to C–OH group stretching (Ahmad et al. 2018). The small peak observed at 894 cm^{-1} indicates the presence of β -(1-4)-glycosidic bonds present in the middle of sugar units (Scheufele et al. 2015).

In the HB spectrum, the bands due to oxygen-containing groups shift to lower wavenumbers, indicating interaction between the organic component and the NPs. Thus, it is observed that the hydroxyl and the carbonyl bands appear at 3314 and 1716 cm^{-1} , respectively.

SEM/EDS analysis

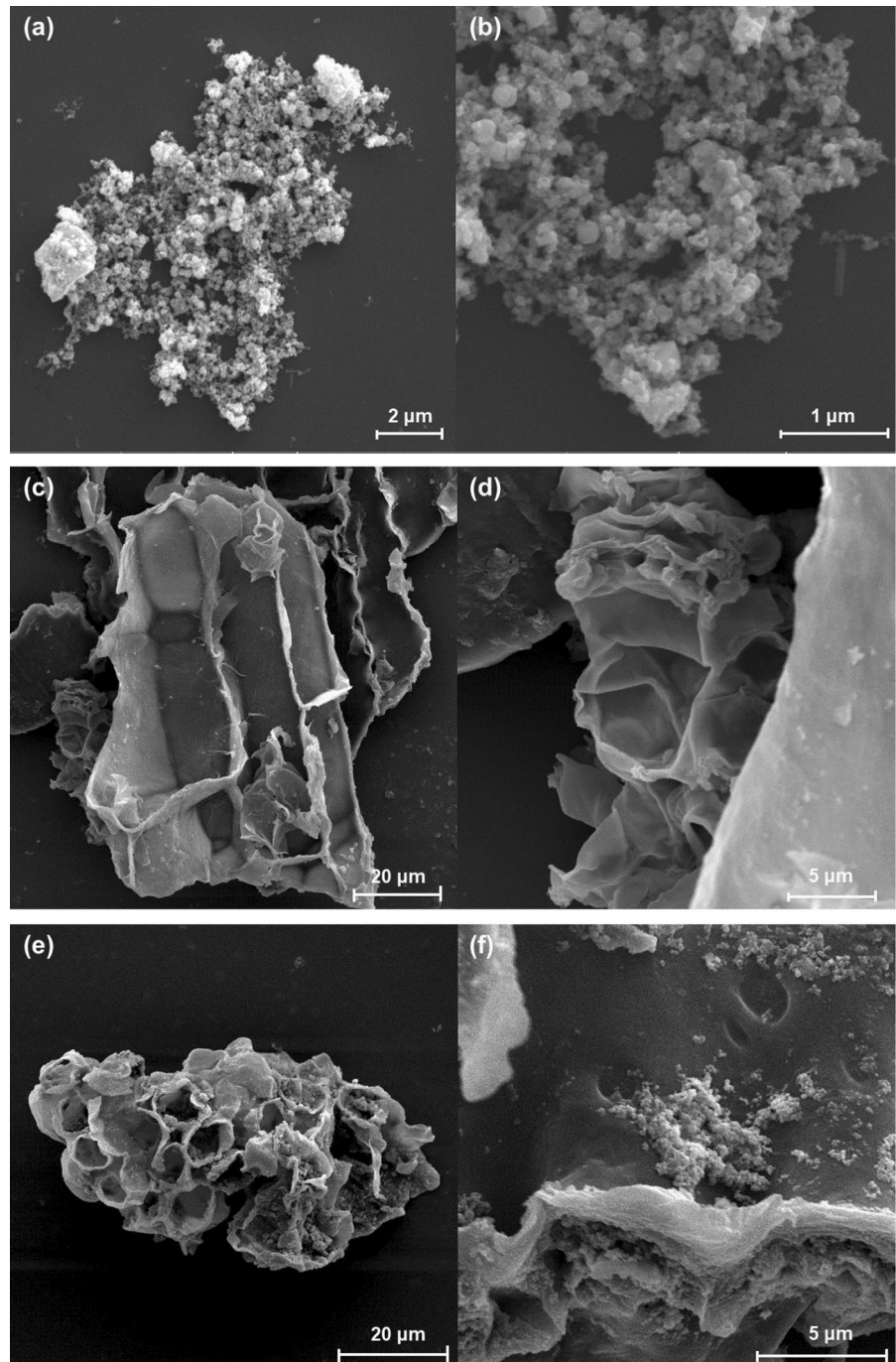
The surface morphology of the NPs, CN and HB samples were analyzed by SEM. The micrographs are shown in Fig. 4.

The SEM images of NPs obtained at a magnification of 15,000 times (Fig. 4a) shows clusters of polydisperse particles. In the image obtained at 100,000 magnification times (Fig. 4b), it is possible to observe clusters of particles of various sizes: while some are smaller than 50 nm , several of them exceed 150 nm . Since these NPs are magnetic, they commonly agglomerate when dispersed in a liquid medium (De Araújo 2011). The SEM images of CN material are shown in Fig. 4c, d. Longitudinal fibrous features from organic matter is revealed (Jawaid et al. 2021). The SEM images of the HB material are presented in Fig. 4e, f. A relevant change in the morphology of the material, when compared to its precursors (NPs and CN), is noticed. The images show that the HB material has a globular morphology, sometimes presenting irregular shapes, with a large size range (from less than 500 nm to about $2\text{ }\mu\text{m}$). EDS analysis did not show any signal from iron in the HB material. However, since the material presented significant attraction to an external magnetic field, the presence of iron in it is clear. The XRD results also support this statement.

Thermal characterization

The thermal stability and mass loss profile of NPs, CN and HB were analyzed in the range of 26 – 900°C . Figure 5 shows the thermograms obtained for the three materials. For the NPs, an initial mass loss takes place between 30 and 100°C , which corresponds to the evaporation of adsorbed water. A second thermal

Fig. 4 SEM images of **a, b** NPs, **c, d** CN, and **e, f** HB material



event occurs between 100 and 300 °C and it is associated with the loss of water molecules more strongly bonded to the NPs. The total percentage of mass loss for the NPs was around 14%. As expected, no further significant loss is observed up to 900 °C.

The CN thermogram was consistent with that found in the literature (Rodríguez-Díaz et al. 2015). According to Machado et al. (Machado et al. 2018) three mass loss events are found for sugarcane bagasse: the loss of surface water around 100 °C, the decomposition of organic matter between 250 and

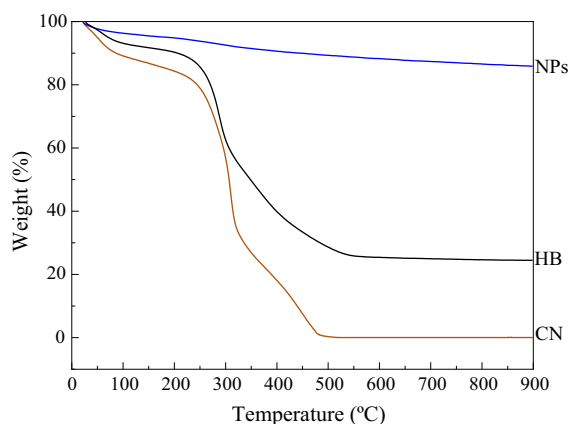


Fig. 5 TGA results for NPs, CN, and HB material

350 °C, and the carbonization of the material between 350 and 480 °C. In this work, the TGA for CN also showed three mass loss events. The first event starts at 30 °C and goes up to 150 °C due to water loss (~7%), the second one goes from 170 to 340 °C due to decomposition of organic matter (~52%) and the last one occurs between 340 and 560 °C, which is attributed to the material carbonization (~35%).

The thermogram obtained for HB was also similar to pyrolyzed organic materials found in the literature (Batra et al. 2008; Rodríguez-Díaz et al. 2015). The first event of mass loss (~3%) occurred between 25 and 100 °C, probably due to moisture loss. The second event (~32%), due to organic decomposition, occurred between 200 and 340 °C, and the third one (~49%), also due to decomposition, occurred between 340 and 550 °C. The similarities between the thermograms of CN and HB can be understood as being due to the low temperatures used in the hydrothermal conditions for the nanohybrid (150 °C) synthesis. This suggests that uncarbonized organic material still exists in HB. The lower amounts of mass loss and the residue observed for HB (~24%) are due to the inorganic NP fraction present.

PZC analysis

The PZC analysis was used to study the surface ability to equally adsorb negative and positive charges. The zero-charge point can be defined as the pH value in which adsorption of H^+ and OH^- ions on the material surface are equal (Kosmulski 2011, 2016). The

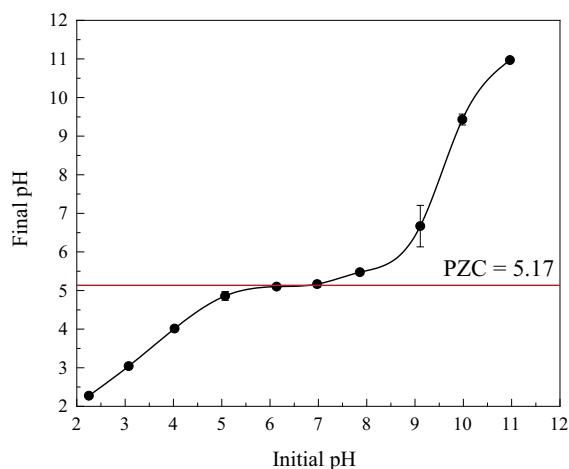


Fig. 6 Point of zero charge for HB material

PZC determination for HB is shown in Fig. 6 and is equal to 5.17, which means that the HB surface is electrically neutral at this pH value.

Thus, the HB surface is negatively charged at pH values higher than 5, presenting cation exchange capacity, whilst it is positively charged when the pH is lower than 5, indicating anion exchange capacity.

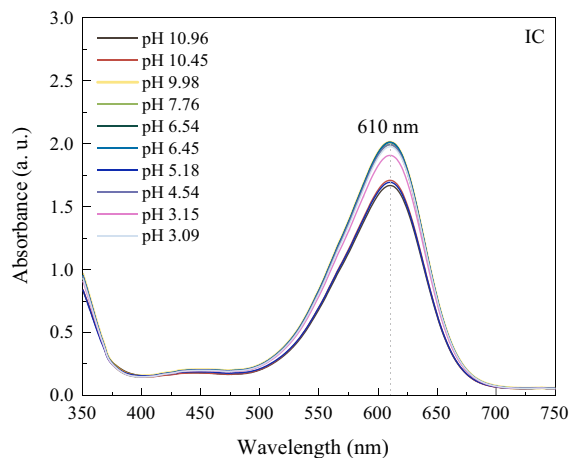


Fig. 7 Study of IC dye stability at pH from 10.96 to 3.09

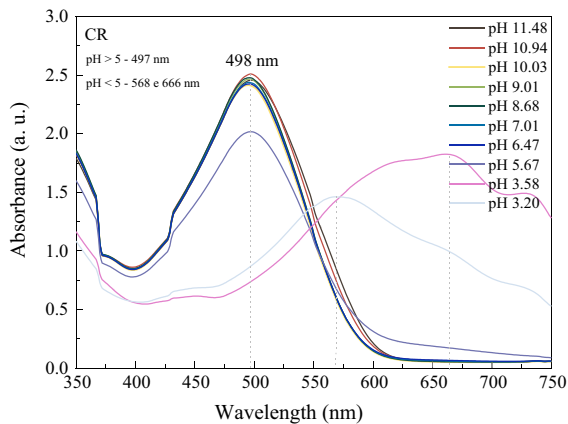


Fig. 8 Study of CR dye stability at pH from 11.48 to 3.20

Table 4 Analysis of ideal pH for IC and CR dyes adsorption

DYES	pH	%R (%) ^a
Indigo carmine	10	29.2
	4	16.9
Congo red	10	22.7
	7	39.1

^a%R (%) = adsorption efficiency

Adsorption application

Effect of pH on indigo carmine and congo red dyes

Indigo carmine and congo red are acid–base indicator dyes, in aqueous solution (Mera and Davies 1984; Zanoni et al. 2010). Their color and absorption characteristics depend on the pH. In the adsorption process, the absorption properties are also governed by the nature of the adsorbent and medium environment.

Figures 7 and 8 show the absorption spectra (350–750 nm) for aqueous solutions of IC and CR, respectively, at various pH values.

The IC dye presents a maximum absorbance wavelength (λ_{\max}) around 610 nm, which does not shift when the pH is varied from ~11 to ~3.0. Color change (from blue to yellow) takes place only above pH 13.

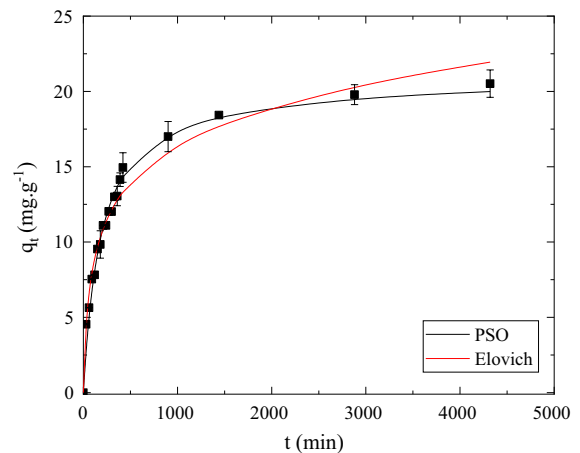


Fig. 9 Adsorption kinetics results for the HB/CR system and fitting of PSO and Elovich models. [CR] = 50.0 mg L⁻¹, mass of HB = 10 mg, room temperature, pH 7.0, 700 rpm

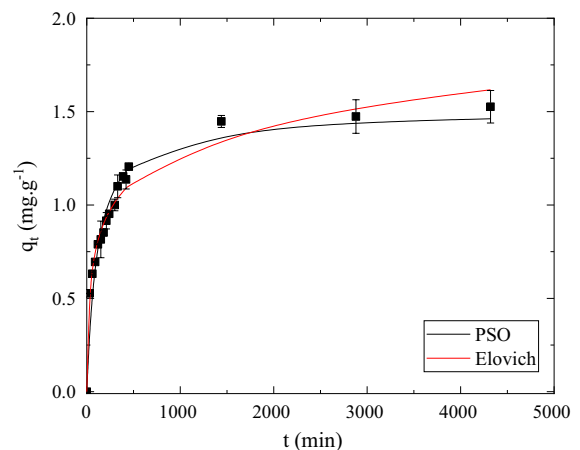


Fig. 10 Adsorption kinetics results for the HB/IC system and fitting of PSO and Elovich models. [IC] = 10.0 mg L⁻¹, mass of HB = 10 mg, room temperature, pH 10.0, 700 rpm

For the CR dye, when the pH is varied from 10.03 to 5.67, λ_{\max} is around 498 nm. It shifts to 568 nm and 666 nm when pH is 3.20 and 3.58. It is known that CR is red at pH above 5.2, changing to blue below 3.0.

Because of the behavior observed for each dye, all experiments with IC were at pH values below 11, while the experiments with CR were at pH values above 5. It is also worth mentioning that both aqueous and buffer solutions of IC and CR were stable for several days.

Table 4 presents the percentual adsorption values for HB/IC at pH 4.0 and 10.0, and for HB/CR in pH 7.0 and 10.0. For CR, the best percentual adsorption (~39%) was obtained for the lower pH (7.0). The highest percentual adsorption for IC (~29%) was obtained in pH 10.0.

Based on these results, all subsequent experiments to study the adsorption of the dyes by HB were carried out using buffer solutions with pH 10.0 (for IC) and 7.0 (for CR). The studies were carried out at pH above the adsorbent's PZC to favor ionic change capacity.

Adsorption kinetics

For the kinetic study, the adsorbent (HB) was added into CR (50 mg L⁻¹) and IC (10 mg L⁻¹) solutions. Figures 9 and 10 show the kinetic data for the HB/CR and HB/IC systems, respectively. For IC, a secondary effect was detected—possibly related to the decomposition of the dye in the presence of HB—which was accentuated after 72 h of contact. For this reason, the kinetic models test was performed only for data

obtained up to 72 h. The complete data, evidencing the observed effect, are presented in the Supporting Information.

Five different kinetic models were used to fit the kinetic data. Table 5 lists the parameters obtained from each model for HB/CR and HB/IC. The pseudo-second order (PSO) model and the Elovich model are used to fit the data in Figs. 9 and 10. The unfitted data are shown in the Supporting Information.

The results observed in Table 5 indicate good fits of the experimental data only for the PSO and Elovich models ($R_{adj}^2 \geq 0.90$), for both dyes. The other investigated models, therefore, cannot be used to predict the adsorption behavior of these dyes, and the phenomena associated to them should not represent how the process is occurring (effects of diffusion resistance are negligible).

A good fit to the PSO model (Wang and Guo 2020) indicates a longer adsorption equilibrium, and the existence of many adsorption sites on the adsorbent. The Elovich model indicates that the activation energy increases with the adsorption time, and that

Table 5 Parameters of the kinetic models applied to the adsorption of CR and IC by HB

Model	Parameter	CR	IC
PFO	q_e (mg g ⁻¹)	12.34 ± 1.08	1.01 ± 0.07
	k_1 (min ⁻¹)	12.31 ± 0.00	1.31 ± 0.00
	R_{adj}^2	0.1975	0.3331
	RMSE	82.2918	0.3287
PSO	q_e (mg g ⁻¹)	20.86 ± 1.94	1.50 ± 0.05
	k_2 (g mg ⁻¹ min ⁻¹)	(2.53 ± 0.19) × 10 ⁻⁴	(5.87 ± 0.83) × 10 ⁻³
	R_{adj}^2	0.9876	0.9599
	RMSE	1.4443	0.0222
Elovich	α (mg g ⁻¹ min ⁻¹)	0.31 ± 0.04	0.07 ± 0.01
	β (g mg ⁻¹)	0.28 ± 0.01	4.41 ± 0.24
	R_{adj}^2	0.9766	0.9760
	RMSE	2.4068	0.0118
IMT	k_{int} (min ⁻¹)	7.93 ± 0.00	2.52 ± 349.94
	q_{max} (mg g ⁻¹)	12.48 ± 175.09	1.05 ± 86.45
	K_L (L mg ⁻¹)	1.77 ± 211.41	0.52 ± 114.79
	R_{adj}^2	0.1440	0.2818
	RMSE	82.2918	0.3287
EMT	k_{ext} (min ⁻¹)	1.66 ± 491.22	1.83 ± 182.14
	q_{max} (mg g ⁻¹)	12.75 ± 210.05	1.04 ± 254.22
	K_L (L mg ⁻¹)	0.61 ± 31.07	0.82 ± 83.96
	R_{adj}^2	0.1441	0.2817
	RMSE	82.2917	0.3286

Table 6 Relevant isotherm parameters derived from IC and CR adsorption onto HB using non-linear Langmuir, Freundlich, Temkin, and Sips models

Model	Parameter	CR			IC		
		25 °C	35 °C	45 °C	25 °C	35 °C	45 °C
Langmuir	q_{mL} ($\text{mg}\cdot\text{g}^{-1}$)	60.41 ± 5.00	70.40 ± 7.31	120.40 ± 19.16	$(9.00 \pm 2.60) \times 10^6$	$(5.28 \pm 1.16) \times 10^6$	$(1.60 \pm 0.71) \times 10^5$
	K_L ($\text{L}\cdot\text{mg}^{-1}$)	$(4.76 \pm 0.97) \times 10^{-2}$	$(5.41 \pm 2.05) \times 10^{-3}$	$(2.62 \pm 1.47) \times 10^{-3}$	$(1.04 \pm 0.29) \times 10^{-6}$	$(2.64 \pm 0.23) \times 10^{-6}$	$(3.13 \pm 0.39) \times 10^{-5}$
	R^2_{adj}	0.9830	0.9382	0.9105	0.9034	0.9059	0.9999
	RMSE	4.7660	13.0090	23.7566	5.4452	3.9280	0.0063
Freundlich	K_F ($\text{mg}\cdot\text{g}^{-1}$)($\text{L}\cdot\text{mg}^{-1}$) $^{1/n_F}$	0.40 ± 0.22	6.15 ± 1.63	6.17 ± 1.10	7.85 ± 1.18	7.02 ± 4.22	5.00 ± 0.00
	n_F	1.10 ± 0.17	2.18 ± 0.35	2.21 ± 0.20	0.66 ± 0.04	0.78 ± 0.14	1.00 ± 0.00
	R^2_{adj}	0.9451	0.9442	0.9769	0.9863	0.9281	0.9999
	RMSE	11.8873	58.6768	32.4585	3.6017	2.7440	0.0001
Temkin	K_T ($\text{L}\cdot\text{g}^{-1}$)	0.50 ± 0.08	0.69 ± 0.28	0.22 ± 0.09	0.44 ± 0.09	0.49 ± 0.15	0.19 ± 0.05
	B ($\text{J}\cdot\text{mol}^{-1}$)	12.99 ± 0.82	10.09 ± 1.56	5.50 ± 1.29	99.48 ± 19.63	94.00 ± 21.65	102.93 ± 16.34
	R^2_{adj}	0.9855	0.9255	0.8019	0.8396	0.8026	0.8981
	RMSE	80.3673	78.4351	42.9267	42.2443	75.3607	56.5221
Sips	q_{mS} ($\text{mg}\cdot\text{g}^{-1}$)	73.79 ± 29.76	100.47 ± 93.60	192.10 ± 109.21	$(4.59 \pm 2.72) \times 10^6$	$(1.34 \pm 0.09) \times 10^6$	$(4.18 \pm 2.08) \times 10^4$
	K_S ($\text{L}\cdot\text{mg}^{-1}$)	$(2.92 \pm 0.97) \times 10^{-2}$	$(8.32 \pm 4.59) \times 10^{-3}$	$(1.42 \pm 0.66) \times 10^{-3}$	$(4.77 \pm 0.97) \times 10^{-6}$	$(7.31 \pm 2.41) \times 10^{-6}$	$(1.23 \pm 0.39) \times 10^{-5}$
	n_S	1.20 ± 0.35	1.61 ± 1.13	1.03 ± 0.66	0.48 ± 0.11	0.78 ± 0.56	0.99 ± 0.02
	R^2_{adj}	0.9809	0.9323	0.9315	0.9872	0.9102	0.9999
	RMSE	21.4817	14.2526	2.9679	0.9845	1.8604	0.0083

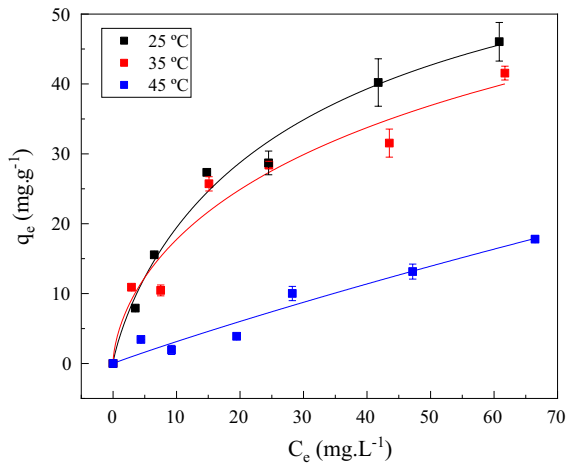


Fig. 11 Adsorption isotherms for the HB/CR system at 25, 35, and 45 °C, with Sips model fitting. Mass of HB: 10.0 mg, pH 7.0, solution volume 50.0 mL; dye concentrations according to Experimental section

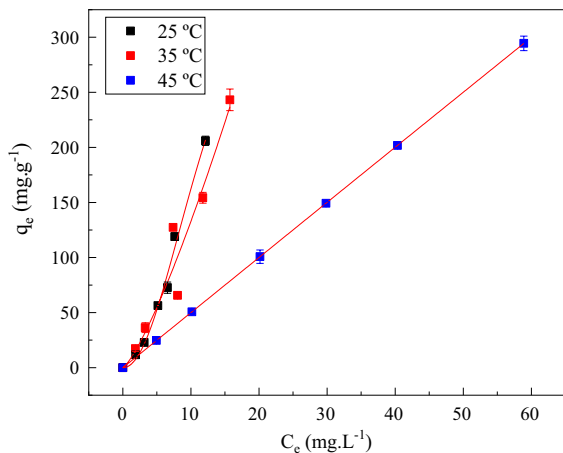


Fig. 12 Adsorption isotherms for the HB/IC system at 25, 35, and 45 °C, with Sips model fitting. Mass of HB: 10.0 mg, pH 10.0, solution volume 50.0 mL; dye concentrations according to Experimental section

the surface of the material is heterogeneous (Wang and Guo 2020). Also, this model suggests that a chemisorptive process is taking place.

The values $q_{e,CR} > q_{e,IC}$ and $k_{2,CR} < k_{2,IC}$ represent a higher amount adsorbed at equilibrium and a slower adsorption of CR compared to IC. In the process investigated in this work, these phenomena seem to be complementary. Although both fitted models can represent the process for the dyes without restrictions,

the PSO model presented lower RMSE values compared to the Elovich model for the HB/CR system. This means that PSO may be more adequate in terms of process description, although effects associated with the Elovich assumptions might also be playing a role. On the other hand, the Elovich model is slightly better for HB/IC—again, with contribution of the PSO characteristics to the kinetics.

Adsorption isotherms

For the study of adsorption equilibrium, Langmuir, Freundlich, Temkin, and Sips models were adjusted to the experimental data (Langmuir 1919; Siddiqui et al. 2018; Damasceno et al. 2020; Yağmur and Kaya 2021).

The Langmuir isotherm describes monolayer coverage of solute on the adsorbent surface at equilibrium, disregarding the interaction among the adsorbed species (Langmuir 1919). The Freundlich isotherm describes the multilayer coverage of solute on the adsorbent surface at equilibrium, considering the adsorption intensity or surface heterogeneity (Proctor and Toro-Vazquez 1996; Abualnaja et al. 2021). The Temkin isotherm describes multilayer coverage of solute on heterogeneous sites of adsorbent, via electrostatic interactions between positive and negative charges, also considering the adsorbate–adsorbate interactions during the adsorption batches (Al-Ghouti and Al-Absi 2020). The Sips isotherm is a combination of Langmuir and Freundlich models. The parameters obtained from the isotherm models are shown in Table 6.

The results presented in Table 6 indicate good fit of the experimental data to the Langmuir, Freundlich and Sips models ($R_{adj}^2 \geq 0.90$), considering the different temperatures, for both dyes. The Temkin model only showed a good fit to the CR dye at temperatures of 25 °C and 35 °C. Even though three models presented good fits to the experimental data, the most suitable for predicting the isotherms is the Sips model, since it presented the lowest RMSE values—and it combines assumptions from Langmuir and Freundlich. Figures 11 and 12 show the isotherms for CR and IC, respectively, at the three temperatures (25, 35, and 45 °C). The Sips fitting is also shown for all isotherms. The other model fittings are shown in the Supporting Information.

From the values obtained for the parameters, it was observed the growth of the maximum amount adsorbed in monolayer for the CR (q_{mL} or q_{mS}), indicating that the filling of the surface for this dye is unfavored by the increase in temperature, while an opposite behavior is observed in the case of IC. The predicted values for the maximum amount adsorbed are much higher for IC compared to CR, but the K_L (and K_S) values are higher for CR, indicating that the

latter tends to reach equilibrium faster, thus promoting less surface filling.

In addition, K_L (and K_S) for CR decreases with increasing the temperature. The opposite behavior is observed for IC. This suggests that the mechanism of adsorption by HB differs for each dye. The values of $n_S \neq 1$ (also seen for n_F) indicate that the process of adsorption displays some heterogeneity, even with $n_S \approx 1$ for IC at 45 °C.

Table 7 Calculated separation factors and adsorption feasibility for HB/IC and HB/CR systems at different temperatures

Parameter	CR			IC		
	25 °C	35 °C	45 °C	25 °C	35 °C	45 °C
K_L (L·mg ⁻¹)	4.76×10^{-2}	5.41×10^{-3}	2.62×10^{-3}	1.04×10^{-6}	2.64×10^{-6}	3.13×10^{-5}
R_L^- (L·mg ⁻¹)	0.81	0.97	0.99	1.00	1.00	1.00
R_L^+ (L·mg ⁻¹)	0.23	0.73	0.85	1.00	1.00	1.00
Feasibility	Favorable	Favorable	Favorable	Linear	Linear	Linear

R_L^- = separator factor calculated based in the lowest dye concentration

R_L^+ (L·mg⁻¹) = separator factor calculated based in the highest dye concentration

Table 8 Thermodynamic parameters for adsorption on first layer

Dye	T(K)	K_S (L·mol ⁻¹)	ΔG (kJ mol ⁻¹)	ΔH (kJ mol ⁻¹)	ΔS (kJ mol ⁻¹ K ⁻¹)	R_{adj}^2	RMSE
CR	298	2.03×10^{-2}	-85.79 ± 17.99				
	308	8.32×10^{-3}	-85.17 ± 17.85	-104.37 ∓ 21.88	-0.06 ∓ 0.02	0.9158	0.1543
	318	1.42×10^{-3}	-84.55 ± 17.72				
IC	298	4.77×10^{-6}	37.31 ± 2.45				
	308	7.31×10^{-6}	32.14 ± 2.44	37.26 ∓ 2.82	0.02 ∓ 0.01	0.9885	0.0264
	318	1.23×10^{-5}	31.97 ± 2.42				

Table 9 Comparison of various adsorbents maximum adsorption capacity on the IC and CR dyes removal

Adsorbent	Adsorbate	pH	Q_m (mg g ⁻¹)	Adsorption time (h)	Ref
Activated carbon	IC	2	9.39	2.5	Bhowmik et al. (2021)
Abrasive spherical materials made of rice husk ash	IC	–	0.40	5	Arenas et al. (2017)
FSB@600 °C-Fe ₃ O ₄	IC	2	7.65	2	Achieng' et al. (2021)
Acacia nilotica sawdust activated carbon	IC	6.76	4.79	2	Gupta and Lataye (2017)
HB nanohybrid	IC	10	1.46	24	This work
MNPs@NiFe LDH	CR	–	79.60	1	Taher et al. (2021)
Fe ₃ O ₄ -AC	CR	4	48.00	1.75	Belachew and Bekele (2020)
MgFe ₂ O ₄ -OH NPs	CR	8	67.60	7	Aoopngan et al. (2019)
Switchgrass-biochar-600 °C	CR	6	8.00	0.25	Park et al. (2019)
HB nanohybrid	CR	7	18.39	24	This work

The findings suggest that adsorption by HB takes place by monolayer formation, and that electrostatic forces might be present. The relatively low values of K_L may indicate that adsorbent and adsorbate interact physically (Langmuir 1919). The separation factor (R_L) was calculated for both systems in the lowest (HB/CR, $C_o=5 \text{ mg L}^{-1}$; HB/IC, $C_o=5 \text{ mg L}^{-1}$) and highest initial concentration (HB/CR, $C_o=70 \text{ mg L}^{-1}$; HB/IC, $C_o=50 \text{ mg L}^{-1}$). The adsorption mechanism of each HB/CR system presented R_L between 0 and 1, indicating favorable adsorptions. On the other hand, each HB/IC system presented $R_L=1$ indicating a linear process (Hall et al. 1966; Arenas et al. 2017; Bhowmik et al. 2021). Therefore, the feasibility of the adsorption was determined according to the separation factor of Langmuir and the shape of isotherm curves (Table 7). The convex isotherm curves ($0 < R_L < 1$) show a favorable adsorption (McKay et al. 1982; Ajenifuja et al. 2017; Hu et al. 2018). Additionally, as closer as to vertical axis, more favorable is the adsorption and smaller is the R_L . The value of Q_e increases linearly with the increase in C_e when $R_L=1$.

The thermodynamic parameters were determined by Eq. (15), using the Sips isotherm constant, and are shown in Table 8.

The results indicate that adsorption is exothermic for CR ($\Delta H < 0$) and endothermic for IC ($\Delta H > 0$): with an increase in temperature, adsorption is inhibited for CR, but favored for IC. The observed absolute ΔH values, much greater than 20 kJ mol^{-1} , indicate that the processes are irreversible—suggesting that chemisorption is taking place. For CR, $\Delta G < 0$, which means that adsorption is spontaneous and favorable. Finally, the higher ΔS values indicate lower randomness for the CR-adsorbate interaction.

Effect of temperature on adsorption

It is noticeable from the isotherms and fitted models (Figs. 11, 12, and Supporting Information) that the increase in temperature enhances the adsorption capacity. At the highest experimental concentrations, the adsorption process exhibited better performance for IC adsorption at $45 \text{ }^\circ\text{C}$ (294.39 mg g^{-1}) in comparison to $35 \text{ }^\circ\text{C}$ (243.96 mg g^{-1}) and $25 \text{ }^\circ\text{C}$ (205.53 mg g^{-1}). This is an indication that the adsorption reaction is endothermic and spontaneous (Santos et al. 2017b; Wahab et al. 2017). This means that

the adsorption efficiency rises with an increment of dye molecules mobility of IC, since it actively interacts towards active sites of the adsorbent molecule because of temperature increment.

The uptake of CR by HB, on the other hand, was more favorable at the lowest temperature (45.98 mg g^{-1} for $25 \text{ }^\circ\text{C}$) compared to the higher temperatures ($35 \text{ }^\circ\text{C}$, 41.30 mg g^{-1} , and $45 \text{ }^\circ\text{C}$, 17.93 mg g^{-1}). The reduction of adsorption capacity at higher temperatures is an indication of an exothermic process (Santos et al. 2017b; Wahab et al. 2017). According to adsorption kinetics and isotherm studies, the removal capacity of CR dye is higher owing to its higher affinity to interact with the HB surface than IC.

Comparison with related studies

Table 9 lists the adsorption capacities obtained for the removal of IC and CR dyes based on different adsorbents. Based on the reported results, the HB is inadequate to remove IC dye, however it can be used effectively for the CR adsorption from aqueous solutions as compared to other adsorbent materials.

Conclusions

A magnetic nanohybrid material (HB) was synthesized by a hydrothermal method from pyrolyzed sugarcane straw (CN) and magnetic iron oxide nanoparticles (NPs) precursors.

The materials were characterized by several techniques, and evaluated as adsorbents for congo red (CR) and indigo carmine (IC) by kinetic and isotherm adsorption tests. XRD and FTIR results confirmed that a hybrid material, composed of the NPs and CN, was obtained. FTIR also showed that interaction between the organic component and the NPs takes place in HB. SEM showed that HB exhibited globular morphology, irregular shape, and a wide size range. PZC showed that the surface of HB is neutral at pH 5.17. The best pH for the uptake of CR and IC was between 5.2 (%R ~ 39%) and 10.0 (%R ~ 23%), and at pH above 5.2 (%R ~ 29%), respectively.

Several kinetic and isotherm models were fitted to the adsorption data, in order to better understand the interactions between the nanohybrid and the dyes. The adsorption kinetics followed well both the PSO

and the Elovich models. This suggests that both PSO and Elovich mechanisms seem to be playing a role, albeit with somewhat different contributions, for the adsorption of CR and IC on HB. PSO is slightly better for the HB/CR system, and the parameters obtained indicate that adsorption equilibrium takes longer, with a higher number of adsorption sites, than for IC. On the other hand, Elovich is slightly better for the adsorption of IC, suggesting that there is some degree of chemisorption.

The Sips model, which combines Langmuir and Freundlich models, provided the best fit to the isotherm data for both dyes. From these parameters, it was observed that HB surface coverage is unfavored by the temperature increase in the case of CR, while the opposite is true for IC. The predicted values for the estimated maximum amount adsorbed were much higher for IC, since the results do not indicate the occurrence of material saturation for the investigated concentration range. In this sense, the observed behavior indicates that increasing the initial concentration would still allow a greater amount of dye to be adsorbed at equilibrium.

One can conclude that HB is a promising material for the removal of dyes with the chemical functionalities found in CR and IC, even though some parameters must be improved. The material utilizes sugarcane waste and relatively cheap, easily made iron oxide NPs. The favorable thermodynamics, the possibility of magnetic recovery and the potential for improving adsorptive capacity and kinetics via synthetic adjustments are also attractive features.

Acknowledgments We gratefully acknowledge the financial support from Brazilian agencies Fundação de Amparo a Ciência e Tecnologia do Estado de Pernambuco (APQ 0692-1.06/15), Conselho Nacional de Desenvolvimento Científico e Tecnológico, and Coordenação de Aperfeiçoamento de Pessoal de Nível Superior. We thank Laboratório de Plasmas e Processos, from Instituto Tecnológico de Aeronáutica, Brazil, for providing the analysis on the thermogravimetric analyzer and X-ray diffractometer equipment.

Author contributions All authors contributed to the study conception and design, as well as data analysis. Material preparation and data collection were performed by R.K.doN., B.S.D., A.N.deM, P.H.M.deF., J.V.F.L.C., and A.C.V.da. The first draft of the manuscript was written by R.K.doN., B.S.D., E.H.L.F., and A.C.V.deA., and all authors commented on previous versions of the manuscript. All authors read and approved the final manuscript.

Funding This work was supported by Brazilian agencies Fundação de Amparo a Ciência e Tecnologia do Estado de Pernambuco (FACEPE, Grant Number APQ 0692-1.06/15), Conselho Nacional de Desenvolvimento Científico e Tecnológico (CNPq), and Coordenação de Aperfeiçoamento de Pessoal de Nível Superior (CAPES).

Declarations

Conflict of interest The authors have no competing interests to declare that are relevant to the content of this article.

References

- Abualnaja KM, Alprol AE, Abu-Saied MA et al (2021) Studying the adsorptive behavior of poly(Acrylonitrile-co-styrene) and carbon nanotubes (nanocomposites) impregnated with adsorbent materials towards methyl orange dye. *Nanomaterials* 11:1144. <https://doi.org/10.3390/nano11051144>
- Achieng' GO, Kowenje CO, Lalah JO, Ojwach SO (2021) Synthesis and characterization of FSB@Fe₃O₄ composites and application in removal of indigo carmine dye from industrial wastewaters. *Environ Sci Pollut Res* 28:54876–54890. <https://doi.org/10.1007/s11356-021-14432-1>
- Ahmad S, Wong YC, Veloo KV (2018) Sugarcane bagasse powder as biosorbent for reactive red 120 removals from aqueous solution. *IOP Conf Ser Earth Environ Sci* 140:012027. <https://doi.org/10.1088/1755-1315/140/1/012027>
- Ajenifuja E, Ajao JA, Ajayi EOB (2017) Equilibrium adsorption isotherm studies of Cu(II) and Co(II) in high concentration aqueous solutions on Ag-TiO₂-modified kaolinite ceramic adsorbents. *Appl Water Sci* 7:2279–2286. <https://doi.org/10.1007/s13201-016-0403-6>
- Al-Ghouthi MA, Al-Absi RS (2020) Mechanistic understanding of the adsorption and thermodynamic aspects of cationic methylene blue dye onto cellulosic olive stones biomass from wastewater. *Sci Rep* 10:1–18. <https://doi.org/10.1038/s41598-020-72996-3>
- Aoopngan C, Nonkumwong J, Phumying S et al (2019) Amine-functionalized and hydroxyl-functionalized magnesium ferrite nanoparticles for congo red adsorption. *ACS Appl Nano Mater* 2:5329–5341. <https://doi.org/10.1021/acsanm.9b01305>
- Arenas CN, Vasco A, Betancur M, Martínez JD (2017) Removal of indigo carmine (IC) from aqueous solution by adsorption through abrasive spherical materials made of rice husk ash (RHA). *Process Saf Environ Prot* 106:224–238. <https://doi.org/10.1016/j.psep.2017.01.013>
- Batra VS, Urbonaite S, Svensson G (2008) Characterization of unburned carbon in bagasse fly ash. *Fuel* 87:2972–2976. <https://doi.org/10.1016/j.fuel.2008.04.010>
- Bedia J, Peñas-Garzón M, Gómez-Avilés A et al (2018) A review on the synthesis and characterization of biomass-derived carbons for adsorption of emerging contaminants from water. *C* 4:63. <https://doi.org/10.3390/c4040063>

- Belachew N, Bekele G (2020) Synergy of magnetite intercalated bentonite for enhanced adsorption of congo red dye. *SILICON* 12:603–612. <https://doi.org/10.1007/s12633-019-00152-2>
- Bhowmik S, Chakraborty V, Das P (2021) Batch adsorption of indigo carmine on activated carbon prepared from sawdust: a comparative study and optimization of operating conditions using Response Surface Methodology. *Results Surf Interfaces* 3:100011. <https://doi.org/10.1016/j.rsufi.2021.100011>
- Cornell RM, Schwertmann U (2003) The iron oxides: structure, properties, reactions, occurrences and uses. Wiley
- Cullity BD, Stock SR (2014) Elements of X-ray diffraction, 2nd edn. Michigan
- Damasceno BS, Da Silva AFV, De Araújo ACV (2020) Dye adsorption onto magnetic and superparamagnetic Fe₃O₄ nanoparticles: a detailed comparative study. *J Environ Chem Eng* 8:103994. <https://doi.org/10.1016/j.jece.2020.103994>
- De Araújo ACV (2011) Síntese de nanopartículas de Fe₃O₄, nanocompósitos de Fe₃O₄ com polímeros e materiais carbonáceos. Universidade Federal de Pernambuco, Thesis
- De Gisi S, Lofrano G, Grassi M, Notarnicola M (2016) Characteristics and adsorption capacities of low-cost sorbents for wastewater treatment: a review. *Sustain Mater Technol* 9:10–40. <https://doi.org/10.1016/j.susmat.2016.06.002>
- dos Santos Rocha MSR, Pratto B, de Sousa R et al (2017a) A kinetic model for hydrothermal pretreatment of sugarcane straw. *Bioresour Technol* 228:176–185. <https://doi.org/10.1016/j.biortech.2016.12.087>
- dos Santos RMM, Gonçalves RGL, Constantino VRL et al (2017b) Adsorption of acid yellow 42 dye on calcined layered double hydroxide: effect of time, concentration, pH and temperature. *Appl Clay Sci* 140:132–139. <https://doi.org/10.1016/j.clay.2017.02.005>
- French AD (2014) Idealized powder diffraction patterns for cellulose polymorphs. *Cellulose* 21:885–896. <https://doi.org/10.1007/s10570-013-0030-4>
- Godoy-Jr A, Pereira A, Gomes M et al (2020) Black TiO₂ thin films production using hollow cathode hydrogen plasma treatment: synthesis, material characteristics and photocatalytic activity. *Catalysts* 5:1–8. <https://doi.org/10.3390/catal10030282>
- Gupta TB, Lataye DH (2017) Adsorption of indigo carmine dye onto acacia nilotica (babool) sawdust activated carbon. *J Hazard Toxic Radioact Waste* 21:04017013. [https://doi.org/10.1061/\(asce\)hz.2153-5515.0000365](https://doi.org/10.1061/(asce)hz.2153-5515.0000365)
- Hall KR, Eagleton LC, Acrivos A, Vermeulen T (1966) Pore and solid-diffusion kinetics in fixed-bed adsorption under constant-pattern conditions. *Ind Eng Chem Fundam* 5:212–223. <https://doi.org/10.1021/i160018a011>
- Hasanpour M, Hatami M (2020) Photocatalytic performance of aerogels for organic dyes removal from wastewaters: review study. *J Mol Liq* 309:113094. <https://doi.org/10.1016/j.molliq.2020.113094>
- Hasanpour M, Motahari S, Jing D, Hatami M (2021a) Investigation of operation parameters on the removal efficiency of methyl orange pollutant by cellulose/zinc oxide hybrid aerogel. *Chemosphere* 284:131320. <https://doi.org/10.1016/j.chemosphere.2021.131320>
- Hasanpour M, Motahari S, Jing D, Hatami M (2021b) Investigation of the different morphologies of zinc oxide (ZnO) in cellulose/ZnO hybrid aerogel on the photocatalytic degradation efficiency of methyl orange. *Top Catal*. <https://doi.org/10.1007/s11244-021-01476-3>
- Hu Q, Liu Y, Feng C et al (2018) Predicting equilibrium time by adsorption kinetic equations and modifying Langmuir isotherm by fractal-like approach. *J Mol Liq* 268:728–733. <https://doi.org/10.1016/j.molliq.2018.07.113>
- Jawaid M, Kian LK, Fouad H et al (2021) Morphological, structural, and thermal analysis of three part of Conocarpus cellulosic fibres. *J Mater Res Technol* 10:24–33. <https://doi.org/10.1016/j.jmrt.2020.11.108>
- Kosmulski M (2011) The pH-dependent surface charging and points of zero charge. V. Update. *J Colloid Interface Sci* 353:1–15. <https://doi.org/10.1016/j.jcis.2010.08.023>
- Kosmulski M (2016) Isoelectric points and points of zero charge of metal (hydr)oxides: 50 years after Parks' review. *Adv Colloid Interface Sci* 238:1–61. <https://doi.org/10.1016/j.cis.2016.10.005>
- Langmuir I (1919) The adsorption of gases on plane surfaces of glass, mica and platinum. *J Am Chem Soc* 40:1361–1403. <https://doi.org/10.1021/ja02242a004>
- Li S, Zhang S, Wang X (2008) Fabrication of superhydrophobic cellulose-based materials through a solution-immersion process. *Langmuir* 24:5585–5590. <https://doi.org/10.1021/la800157t>
- Liao Z, Huang Z, Hu H et al (2011) Microscopic structure and properties changes of cassava stillage residue pretreated by mechanical activation. *Bioresour Technol* 102:7953–7958. <https://doi.org/10.1016/j.biortech.2011.05.067>
- Libra JA, Ro KS, Kammann C et al (2011) Hydrothermal carbonization of biomass residuals: a comparative review of the chemistry, processes and applications of wet and dry pyrolysis. *Biofuels* 2:71–106. <https://doi.org/10.4155/bfs.10.81>
- Lopičić ZR, Stojanović MD, Marković SB et al (2019) Effects of different mechanical treatments on structural changes of lignocellulosic waste biomass and subsequent Cu(II) removal kinetics. *Arab J Chem* 12:4091–4103. <https://doi.org/10.1016/j.arabjc.2016.04.005>
- Machado G, Santos F, Faria D et al (2018) Characterization and potential evaluation of residues from the sugarcane industry of Rio Grande do Sul in biorefinery processes. *Nat Resour* 09:175–187. <https://doi.org/10.4236/nr.2018.95011>
- Marković S, Stanković A, Lopičić Z et al (2015) Application of raw peach shell particles for removal of methylene blue. *J Environ Chem Eng* 3:716–724. <https://doi.org/10.1016/j.jece.2015.04.002>
- McKay G, Blair HS, Gardner JR (1982) Adsorption of Dyes on Chitin. *J Appl Polym Sci* 27:3043–3057. https://doi.org/10.1007/978-981-10-6293-3_2
- Mera SL, Davies JD (1984) Differential congo red staining: the effects of pH, non-aqueous solvents and the substrate. *Histochem J* 16:195–210. <https://doi.org/10.1007/BF01003549>
- Nordin AH, Wong S, Ngadi N et al (2021) Surface functionalization of cellulose with polyethyleneimine and magnetic nanoparticles for efficient removal of anionic dye in

- wastewater. *J Environ Chem Eng* 9:104639. <https://doi.org/10.1016/j.jece.2020.104639>
- Park JH, Wang JJ, Meng Y et al (2019) Adsorption/desorption behavior of cationic and anionic dyes by biochars prepared at normal and high pyrolysis temperatures. *Colloids Surf A Physicochem Eng Asp* 572:274–282. <https://doi.org/10.1016/j.colsurfa.2019.04.029>
- Phat LN, Nguyen HC, Khoa BDD et al (2022) Synthesis and surface modification of cellulose cryogels from coconut peat for oil adsorption. *Cellulose* 29:2435–2447. <https://doi.org/10.1007/s10570-022-04427-7>
- Poolwong J, Kiatboonyarit T, Achiwawanich S et al (2021) Three-dimensional hierarchical porous TiO₂ for enhanced adsorption and photocatalytic degradation of remazol dye. *Nanomaterials* 11:1715. <https://doi.org/10.3390/nano11071715>
- Proctor A, Toro-Vazquez JF (1996) The Freundlich isotherm in studying adsorption in oil processing. *J Am Oil Chem Soc* 73:1627–1633. <https://doi.org/10.1007/BF02517963>
- Rodríguez-Díaz JM, García JOP, Sánchez LRB et al (2015) Comprehensive characterization of sugarcane bagasse ash for its use as an adsorbent. *Bioenergy Res* 8:1885–1895. <https://doi.org/10.1007/s12155-015-9646-6>
- Scheufele FB, Ribeiro C, Módenes AN et al (2015) Assessment of drying temperature of sugarcane bagasse on sorption of reactive blue 5G dye. *Fibers Polym* 16:1646–1656. <https://doi.org/10.1007/s12221-015-5087-2>
- Shao X, Wang J, Liu Z et al (2021) Cellulose based cation-exchange fiber as filtration material for the rapid removal of methylene blue from wastewater. *Cellulose* 28:9355–9367. <https://doi.org/10.1007/s10570-021-04103-2>
- Shrestha D (2021) Efficiency of wood-dust of dalbergia sisoo as low-cost adsorbent for rhodamine-B dye removal. *Nanomater* 11:2217. <https://doi.org/10.3390/nano11092217>
- Siddiqui SI, Rathi G, Chaudhry SA (2018) Acid washed black cumin seed powder preparation for adsorption of methylene blue dye from aqueous solution: thermodynamic, kinetic and isotherm studies. *J Mol Liq* 264:275–284. <https://doi.org/10.1016/j.molliq.2018.05.065>
- Srinivasan A, Viraraghavan T (2010) Decolorization of dye wastewaters by biosorbents: a review. *J Environ Manag* 91:1915–1929. <https://doi.org/10.1016/j.jenvman.2010.05.003>
- Taher T, Putra R, Rahayu Palapa N, Lesbani A (2021) Preparation of magnetite-nanoparticle-decorated NiFe layered double hydroxide and its adsorption performance for congo red dye removal. *Chem Phys Lett* 777:138712. <https://doi.org/10.1016/j.cplett.2021.138712>
- Wahab R, Khan F, Kaushik NK et al (2017) Photocatalytic TMO-NMs adsorbent: temperature-time dependent Safranine degradation, sorption study validated under optimized effective equilibrium models parameter with standardized statistical analysis. *Sci Rep* 7:1–15. <https://doi.org/10.1038/srep42509>
- Wang J, Guo X (2020) Adsorption kinetic models: physical meanings, applications, and solving methods. *J Hazard Mater* 390:122156. <https://doi.org/10.1016/j.jhazmat.2020.122156>
- Yağmur HK, Kaya İ (2021) Synthesis and characterization of magnetic ZnCl₂-activated carbon produced from coconut shell for the adsorption of methylene blue. *J Mol Struct* 1232:130071. <https://doi.org/10.1016/j.molstruc.2021.130071>
- Zanoni TB, Cardoso AA, Zanoni MVB, Ferreira AAP (2010) Exploratory study on sequestration of some essential metals by indigo carmine food dye. *Braz J Pharm Sci* 46:723–730. <https://doi.org/10.1590/S1984-82502010000400014>

Publisher's Note Springer Nature remains neutral with regard to jurisdictional claims in published maps and institutional affiliations.

Springer Nature or its licensor (e.g. a society or other partner) holds exclusive rights to this article under a publishing agreement with the author(s) or other rightsholder(s); author self-archiving of the accepted manuscript version of this article is solely governed by the terms of such publishing agreement and applicable law.